

Non-Hermitian boundary spectral winding

Zuxuan Ou,¹ Yucheng Wang,^{2,3,4} and Linhu Li^{1,*}

¹Guangdong Provincial Key Laboratory of Quantum Metrology and Sensing & School of Physics and Astronomy, Sun Yat-Sen University (Zhuhai Campus), Zhuhai 519082, China

²Shenzhen Institute for Quantum Science and Engineering, Southern University of Science and Technology, Shenzhen 518055, China

³International Quantum Academy, Shenzhen 518048, China

⁴Guangdong Provincial Key Laboratory of Quantum Science and Engineering, Southern University of Science and Technology, Shenzhen 518055, China

(Dated: October 25, 2022)

Spectral winding of complex eigenenergies represents a topological aspect unique in non-Hermitian systems, which vanishes in one-dimensional (1D) systems under the open boundary conditions (OBC). In this work, we discover a boundary spectral winding in two-dimensional non-Hermitian systems under the OBC, originating from the interplay between Hermitian boundary localization and non-Hermitian non-reciprocal pumping. Such a nontrivial boundary topology is demonstrated in a non-Hermitian breathing Kagome model with a triangle geometry, whose 1D boundary mimics a 1D non-Hermitian system under the periodic boundary conditions with nontrivial spectral winding. In a trapezoidal geometry, such a boundary spectral winding can even co-exist with corner accumulation of edge states, instead of extended ones along 1D boundary of a triangle geometry. An OBC type of hybrid skin-topological effect may also emerge in a trapezoidal geometry, provided the boundary spectral winding completely vanishes. By studying the Green's function, we unveil that the boundary spectral winding can be detected from a topological response of the system to a local driving field, offering a realistic method to extract the nontrivial boundary topology for experimental studies.

Introduction. - Non-Hermitian systems can support not only topological phases with boundary states protected by conventional band topology [1, 2], but also spectral winding topology of complex eigenenergies which has no Hermitian analogue. Nontrivial spectral winding generally emerges in many non-Hermitian lattices under the periodic boundary conditions (PBC), and vanishes when the boundary is opened (i.e. the open boundary condition, OBC), resulting in the non-Hermitian skin effect (NHSE) where bulk states become skin-localized at the system's boundary [3–7]. One of the most noteworthy consequences of the interplay between conventional and spectral winding topology is the breakdown of conventional topological bulk-boundary correspondence [8, 9], which has led to recent extensive investigations of its recovery through several different methods [3, 10–14] and many other exciting phenomena induced by NHSE and spectral winding topology [15–36].

In contemporary literature, spectral winding topology is mainly studied in one dimensional (1D) systems, as by definition it corresponds to 1D trajectories in the two dimensional (2D) complex-energy plane, which cannot be straightforwardly generalized into higher spatial dimensions. On the other hand, being a boundary phenomenon, NHSE in 2D or higher dimension are also far more sophisticated than in 1D, possessing many variations associated with different boundaries and defects due to their richer geometric structures [37–42]. In this work, we unveil an exotic aspect of spectral winding in higher dimensions, namely nontrivial spectral winding for 1D boundary states of 2D lattices under the OBC, in sharp contrast to our knowledge of vanishing spectral winding topology of OBC systems. Its emergence originates from the interplay between topological boundary localization and a non-Hermitian chiral pumping along the bound-

ary, namely asymmetric hoppings with stronger amplitudes toward a chiral direction [see Fig. 1(a) for an illustration]. A similar mechanism is known to be responsible for the hybrid skin-topological effect (HSTE) [43–46], a type of higher-order NHSE with topological protection [47–49], which induces corner skin-topological localization in 2D lattices. Interestingly, our example model of non-Hermitian breathing Kagome lattice can support both nontrivial boundary spectral winding and an OBC type of HSTE under the same parameters, but with different triangle and trapezoidal geometries, where the chiral pumping is destroyed by geometric properties of the latter case. In the intermedia regime between these two scenarios, nontrivial boundary spectral winding may even coincide with a weak corner localization, indicating an anomalous co-existence of the seemingly contradictory boundary spectral winding and HSTE, which require rather different geometric properties along boundaries. Moreover, we discover that this boundary spectral winding can be detected from a topological response to a driving field when locally perturbing the 2D system, providing a feasible method to extract the nontrivial boundary topology from realistic non-Hermitian systems.

Non-Hermitian breathing Kagome model. - We consider a non-Hermitian breathing Kagome model with asymmetric intracell hoppings as shown in Fig.1(a), with its bulk Hamiltonian given by

$$H(\mathbf{k}) = \begin{pmatrix} 0 & t_a + t_b^+ e^{-ik_1} & t_a + t_b^- e^{ik_3} \\ t_a + t_b^- e^{ik_1} & 0 & t_a + t_b^+ e^{-ik_2} \\ t_a + t_b^+ e^{-ik_3} & t_a + t_b^- e^{ik_2} & 0 \end{pmatrix}, \quad (1)$$

where $k_1 = -k_x/2 - \sqrt{3}k_y/2$, $k_2 = k_x$ and $k_3 = -k_x/2 + \sqrt{3}k_y/2$, $t_b^\pm = t_b e^{\pm\alpha}$ represent asymmetric intercell (upward triangle) hopping parameters, and t_a is the amplitude of intracell

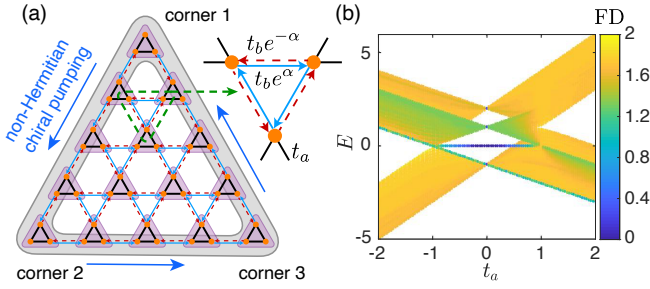


FIG. 1. (a) A sketch of the non-Hermitian breathing Kagome lattice with $L = 5$ rows of unit cells. Gray area represents the 1st-order boundary of the system, which gives the effective boundary Hamiltonian discussed later. Blue arrows indicate the direction of non-Hermitian chiral pumping along the boundary. (b) Energy spectrum versus t_a , for the system with a triangle geometry in the Hermitian limit of $\alpha = 0$. Eigenenergies are marked by different colors according to their corresponding FD. Other parameters are $t_b = 1$ and $L = 30$.

(downward triangle) Hermitian hopping. Here we set $t_b = 1$ as the unit energy. In the Hermitian scenario with $\alpha = 0$, the Kagome lattice model supports both 1st-order edge states and 2nd-order corner states in certain parameter regimes, as shown in Fig. 1(b) where different bulk and boundary states are characterized by different values of their fractal dimension (FD), defined as

$$\text{FD} = -\ln\left[\sum_{\mathbf{r}} |\psi_{n,\mathbf{r}}|^4\right] / \ln \sqrt{3N}, \quad (2)$$

with $\psi_{n,\mathbf{r}}$ the wave amplitude at position \mathbf{r} of the n -th eigenstate, and N the total number of unit cells. In a triangle geometry, $N = (1 + L)L/2$ with L the number of rows of unit cells in the lattice. A 2D bulk state and a 1D edge state in our system shall have their FD close to 2 and 1 respectively. As seen in Fig. 1(b), the breathing Kagome lattice supports 1D edge states (represented by green color for $\text{FD} \approx 1.2$) in a large parameter regime.

Destructive interference of non-reciprocity and boundary spectral winding.- By construction, the model can be viewed as a combination of three sets of non-Hermitian Su-Schrieffer-Heeger (SSH) chains [3, 50–52] along different directions. Specifically, the three non-Hermitian SSH chains are chosen to be identical, resulting in a C_3 rotation symmetry of the system, as shown in Fig. 1(a). In this way, the asymmetric hoppings along the three directions form a closed loop and balance out in each unit cell, leading to a destructive interference of non-reciprocity in the bulk. The system is thus net-reciprocal even in the presence of asymmetric hoppings. As seen in Fig. 2(a), FD is close to 2 for eigenstates in three bulk bands (yellow color) for the system with a triangle geometry, indicating the absence of NHSE for bulk states. Consistently, the summed bulk distribution, defined as

$$\rho_{\text{bulk}}(\mathbf{r}) = \sum_{n \in \text{bulk}} |\psi_{n,\mathbf{r}}|^2$$

with summation runs over all eigenstates in the bulk bands,

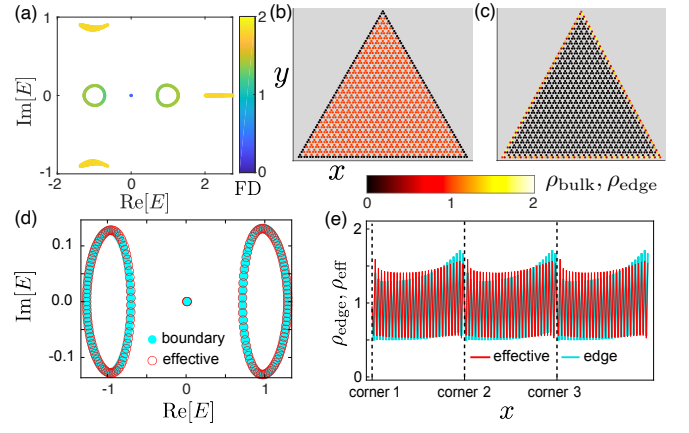


FIG. 2. (a) Energy spectrum under the OBC, colors indicate the FD of each eigenstate. (b) and (c) Summed distribution of bulk states and edge states respectively. (d) Spectra of edge states for the 2D lattice (cyan dots) as in (a), and 1D effective boundary system corresponding to the gray area in Fig. 1(a) (red circles). (e) Summed distribution of edge states for the 2D lattice (cyan), and of all eigenstates for the 1D boundary system (red). Parameters are $t_a = 0.25$, $t_b = 1$, $\alpha = 0.5$, $L = 30$.

also distributes uniformly in the 2D bulk [Fig. 2(b)]. On the other hand, 1st-order edge states distribute mostly along 1D edges, and are subjected to a net non-Hermitian non-reciprocal pumping. The same mechanism is known to induce the HSTE in different square and honeycomb lattices. However, in our model with a triangle geometry, the destructive interference of non-reciprocity limits the choices of the non-reciprocal directions and forbids the HSTE. Namely, in the presence of destructive interference of non-reciprocity along three directions, a triangle lattice must have chiral non-reciprocal pumping along its 1D boundary, hence it is impossible to have two edges with non-reciprocity toward their shared corner. Consequently, we anticipate no hybrid skin-topological corner mode to appear in our system.

As verified in our numerical calculations, 1st-order edge states are indeed extended along 1D edges, as shown in Fig. 2(c) by the summed edge distribution

$$\rho_{\text{edge}}(\mathbf{r}) = \sum_{n \in \text{edge}} |\psi_{n,\mathbf{r}}|^2$$

with summation runs over all edge states. Interestingly, a non-trivial spectral winding is seen to emerge for edge states, even when the system is under OBC [Fig. 2(a)]. To understand its emergence, we note that these edge states inhabit within the edges of a 2D lattice, which form an effective 1D boundary system without an open boundary, analogous to a 1D non-reciprocal system under PBC. By taking the edges of the 2D lattice as a 1D system decoupled from the 2D bulk, we find that its spectrum is almost identical to that of the 1st-order edge states of the original 2D system, as shown in Fig. 2(d). As seen in Fig. 2(e), their eigenstates display a slightly different but still extended distribution, as shown by $\rho_{\text{eff}} = \sum_n |\psi_{n,x}^{\text{1D}}|^2$

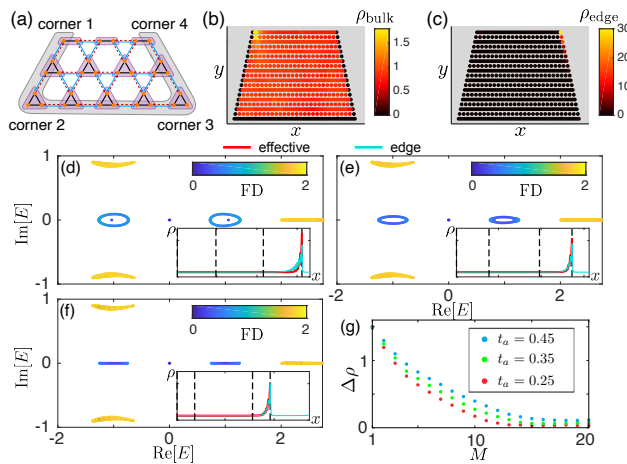


FIG. 3. (a) A sketch of a trapezoidal lattice of the non-Hermitian breathing Kagome model. (b) and (c) Summed distribution of bulk states and edge states respectively, with $L = 30$ and $M = 20$. (d) to (f) Energy spectra under OBC with $L = 30$, and $M = 5, 10, 20$ respectively, colors indicate the FD of each eigenstate. Summed distributions of edge states for the 2D trapezoidal lattice in (d) to (e) are illustrated in their insets (cyan), together with that of all eigenstates for the 1D boundary system (red). Dash lines correspond to corners 1 to 4 from left to right respectively. (g) $\Delta\rho = \sum_x |\rho_{\text{eff}} - \rho_{\text{edge}}|/L_{\text{eff}}$ as a function of M , for several different values of t_a . $t_a = 0.25$ is chosen in (b) to (f). Other parameters are $t_b = 1, \alpha = 0.5$.

with $\psi_{n,x}^{\text{1D}}$ the wave amplitude at position x of the n -th eigenstate of the 1D boundary system. Thus, the origin of nontrivial boundary spectral winding in our model can be qualitatively understood from this 1D boundary system. Note that in contrast to an actual 1D PBC system, 1D edges of our 2D model possess an extra lattice site in each corner, acting as impurities to the 1D effective model. As a result, we observe weak eigenstate accumulations toward these corners for both the edge states of the 2D model, and for the effective 1D boundary system [Fig. 2(e)].

Trapezoidal lattices and an OBC type of hybrid skin-topological localization.- In the triangle lattice, the emergence of nontrivial boundary spectral winding relies on the chiral non-reciprocal pumping along 1D boundary. To further confirm this mechanism, here we break the chiral pumping channel by removing top few rows of lattice sites from the triangle lattice. Specifically, we start from a triangle lattice with L unit cells along its bottom row, then remove top M rows of unit cells, and the top lattice sites of unit cells in the $M + 1$ row. A sketch of $L = 5$ and $M = 2$ is shown in Fig. 3(a). In the resultant trapezoidal lattices, the top row of lattice sites do not form complete upward unit cells, and asymmetric hoppings between these sites have stronger amplitudes toward the opposite chiral direction of the rest three edges, blocking the chiral pumping channel circulating the 2D lattice.

Intuitively, two domain-walls are formed between top and rest edges at corners 1 and 4, which shall leads to the emergence of HSTE in the trapezoidal geometry of our model. Yet its behaviors cannot be simply understood from this domain-

wall picture. To see this, we may redefine a unit cell as a downward triangle [i.e. the green dash line in Fig. 1(a)]. Then, when excluding the boundary lattice sites of left, right, and bottom edges, the rest part of a trapezoidal lattice is formed only by intact unit cells. Therefore the top geometric edge of a trapezoidal lattice is more closely related to the physical bulk, and shall be considered as a part of it. In return, the effective 1D boundary no longer forms a closed loop. Indeed, as observed in Fig. 3(b) with $L = 30$ and $M = 20$, bulk states of the system show vanishing distribution only along the left, right, and bottom edges. On the other hand, edge states in this system exhibit a clear accumulation at top-right corner (corner 4) for the chosen parameters, in analog to the behavior of a 1D non-Hermitian OBC system with the NHSE.

To further understand the boundary behaviors, we demonstrate the energy spectra for lattices with different sizes in Figs. 3(d)-(f), with insets illustrating the distributions of their edge states and of a 1D boundary system under the OBC [i.e. the gray area in Figs. 3(a)]. In Figs. 3(d), the top $M = 5$ rows of unit cells are removed from a triangle lattice with $L = 30$. The resultant system shows a nontrivial boundary spectral winding in its complex spectrum, yet its edge states already become corner-localized (with FD close to 0) and accumulate at corner 4. However, their accumulating strength is considerably weaker than that of skin states of the effective 1D OBC system. Such observations are in analogous to the scale-free localization induced by impurities in a 1D non-Hermitian chain, where a boundary impurity connects the 1D chain head to tail, resulting in an impurity boundary condition (IBC) between the OBC and PBC [30]. In our trapezoidal lattice, the top row of lattice sites can be viewed as impurities connecting the two ends (i.e. corners 1 and 4) of the 1D edges, mimicking the IBC that gives rise to the scale-free localization.

In Figs. 3(e), we demonstrate results with the same number of unit cells in the bottom row ($L = 30$), but removing the top $M = 10$ rows from a triangle lattice. Its edge states still form a loop-spectrum in the complex plane, yet their distribution becomes closer to the skin states of the corresponding 1D boundary system under the OBC. Finally, when further removing more rows from the triangle lattice [$M = 20$ in Fig. 3(f)], the boundary spectral winding eventually vanishes, and the distribution of edge states become almost identical to the skin states. It indicates that the boundary of the 2D trapezoidal lattice becomes an analog of an 1D OBC chain, and supports an OBC type of HSTE, with a vanishing distribution on the other side of the corner, i.e. lattice sites in the top geometric edge of the trapezoidal lattice. This is because these sites act as a part of the bulk and hence behave as a vacuum for the skin-topological states. To characterize this geometry-dependent behavior, we demonstrate the difference between ρ_{eff} and ρ_{edge} in Fig. 3(g), defined as

$$\Delta\rho = \sum_x |\rho_{\text{eff}} - \rho_{\text{edge}}|/L_{\text{eff}}$$

with L_{eff} the size of the 1D boundary system. It is seen that $\Delta\rho$ reaches its minimal value at around $M = 15$ for $t_a = 0.25$, the

parameter chosen in other figures. With larger t_a , edge states of breathing Kagome lattice become less localized along its 1D boundary, and their distributions also slightly diverge from that of the 1D boundary system, as shown by the increasing minimal value of $\Delta\rho$ in Fig. 3(g). In Supplemental Materials [53], we further demonstrate examples of hexagon lattices, which also exhibit HSTE and boundary spectral winding similar to trapezoid lattices, and effective OBC and IBC for their 1D edges can be more clearly identified from a Green's function analysis.

Detection of boundary spectral winding through a topological response.- In 1D non-Hermitian systems, it has been recently revealed that nontrivial spectral winding has a one-to-one correspondence to a quantized quantity in the response to an external local driving field [33]. Since edge states of our 2D model effectively give a 1D boundary system, we expect that such a topological response corresponding to spectral winding also emerges here. Specifically, The topological response quantity is defined as

$$\nu_{mn}(\beta) = \partial \ln |G_{mn}(\beta)| / \partial \beta,$$

with β describing a perturbation to the amplitude of one intracell hopping along the system's 1D boundary $t_a \rightarrow t_a e^{-\beta}$, $G(\beta) = 1/[E_r - H(\beta)]$ the Green's function regarding a reference energy E_r , and (m, n) labeling the two sites connected by the perturbed hopping. We note that to obtain a topological response for the boundary spectral winding, the modified hopping can be chosen arbitrarily from the 1D boundary for the triangle lattice, but cannot be chosen from the top row of a trapezoidal lattice, which belongs to the bulk system [53]. In the following discussion, it is chosen to locate at the center of the bottom boundary. Physically, $|G_{mn}(\beta)|$ describes the amplitude of a response at site m to a local driving field at site n [20], thus $\nu_{mn}(\beta)$ describes the changing rate of this response strength with varying β [53].

We first consider the triangle lattice with the same parameters as in Fig. 2. As seen in Fig. 4(a) and (b), $G_{mn}(\beta)$ and $\nu_{mn}(\beta)$ behave rather differently for reference energies inside (blue) and outside (red) the loops of boundary spectrum. For the former case, $|G_{mn}(\beta)|$ increases with β and eventually stops at a large constant value ($\sim e^5$), analogous to the direction signal amplification 1D non-Hermitian system [19, 20]. In contrast, $|G_{mn}(\beta)|$ decreases to a small value ($\sim e^{-3}$) for a reference energy outside the loops of boundary spectrum. More importantly, it is seen that $\nu_{mn}(\beta) \simeq 1$ ($\nu_{mn}(\beta) \leq 0$) for small β when E_r is (not) enclosed by the loops of boundary spectrum, in consistent with the quantized topological response in actual 1D systems [33–35]. Therefore we scan E_r for a parameter regime covering the system's full spectrum, and demonstrate the value of $\nu_{mn}(\beta)$ at $\beta = 0$ in Fig. 4(c). As seen in the results, the region with nontrivial boundary spectral winding is characterized by $\nu_{mn}(0) \simeq 1$, while other regions generally have a non-positive $\nu_{mn}(0)$. Furthermore, in Figs. 4(e) and (f) we demonstrate the same response quantity $\nu_{mn}(\beta)$ for trapezoidal lattices with the same lattice size and parameters as in Figs. 3(d) to (f). The nontrivial region is seen to shrink and

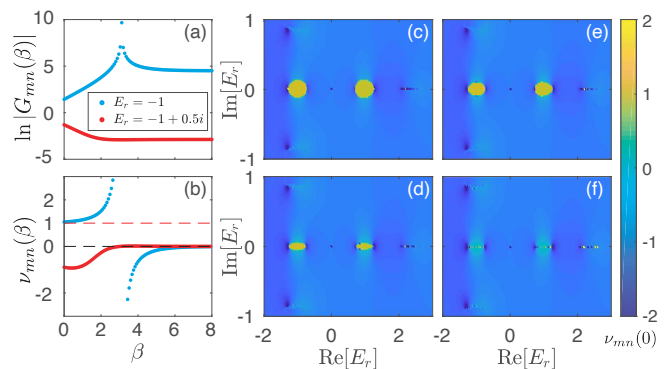


FIG. 4. (a) Element $G_{mn}(\beta)$ of the Green's function for the triangle lattice with the same parameters as in Fig. 1(a), for different reference energies E_r enclosed by the loop-like boundary spectrum (blue dots), and within the gap (red dots) respectively. (b) Topological response $\nu_{mn}(\beta)$ for the same system and parameters as in (a). (c) to (f) Topological response $\nu_{mn}(\beta)$ at $\beta = 0$ for (c) the triangle lattice with $L = 30$ rows of unit cells, and (d)-(f) the trapezoidal lattices with for Fig. 3(d) to (f) $M = 5, 10, 20$ rows removed from the triangle lattice respectively. In all these results, m and n are chosen as the bottom-left and -right sites of the 15th unit cell in the bottom row of the lattices.

disappear for trapezoidal lattices when removing more rows of unit cells, which perfectly matches the boundary spectra displayed in Figs. 3(d) to (f).

Conclusion.- In summary, we highlight a boundary spectral winding in 2D non-Hermitian systems under the OBC, originating from the interplay between Hermitian (topological) boundary localization and non-Hermitian non-reciprocal pumping. The mechanism is similar to that of the HSTE, yet these two phenomena require rather different boundary geometric properties. Specifically, nontrivial boundary spectral winding naturally arises in a triangle lattice of a non-Hermitian breathing Kagome model, where a destructive interference of non-reciprocity along three directions ensures chiral non-reciprocal pumping along the 1D boundary of the lattice. On the other hand, a trapezoidal lattice of the same model supports different directions of non-reciprocal pumping for different parts of its boundary, leading to either a boundary spectral winding with a weak corner localization of edge states, or an OBC type of HSTE, depending on the exact shape of the trapezoidal lattice. In both cases, we find that the boundary spectral winding can be detected from a topological response to a local driving field in the presence of a local boundary perturbation, established from an element of the Green's function matrix associating the response and the driven lattice sites. Our model is readily for experimental realization with RLC circuit lattices, as it is constructed with the same hopping components as a non-Hermitian 2D lattice already realized in this platform [54]. The topological response ν_{mn} can also be detected in such systems by measuring the two-point impedance between sites m and n [33]. We also note that while this work has focused on a non-Hermitian breathing

Kagome model with different geometries, the boundary spectral winding also emerges in other models and geometries, and we have demonstrated several examples in the Supplemental Materials [53].

L. L. would like to thank C. H. Lee, J. Gong, and W. Zhu for helpful discussion. This work is supported by the National Natural Science Foundation of China (12104519) and the Guangdong Basic and Applied Basic Research Foundation (2020A1515110773).

Supplementary Materials for “Non-Hermitian boundary spectral winding”

HEXAGONAL GEOMETRIES OF THE NON-HERMITIAN BREATHING KAGOME MODEL

In the main text, we have taken a non-Hermitian breathing Kagome model as an example, where nontrivial boundary spectral winding emerges with triangle and some trapezoidal geometries. More generally, boundary spectral winding can be expected also in other geometries or other 2D non-Hermitian models, as long as chiral non-reciprocal pumping dominates its 1D boundary. In this section, we shall demonstrate extra examples of this model with hexagonal geometries, which can be obtained from the triangle lattice by removing a few rows of lattice sites from each corner. Specially, we start from a triangle lattice with L unit cells along its bottom row, then remove top Q rows of unit cells, and the top lattice sites of unit cells in the $Q + 1$ row on each corner.

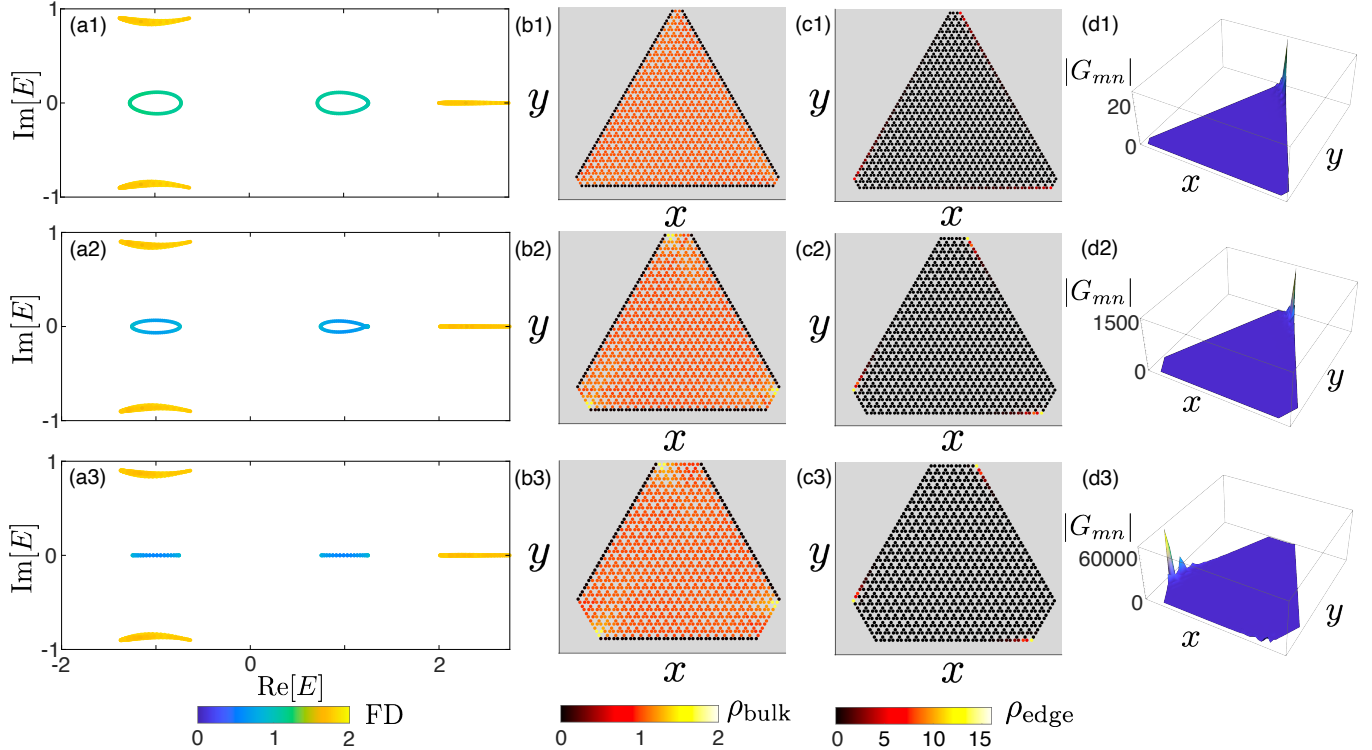


FIG. S1. (a1) to (a3) Energy spectra of hexagonal lattices with $L = 30$, and $Q = 1, 3, 5$ respectively, colors indicate the FD of each eigenstate. (b1) to (b3) Summed distribution of bulk states in (a1) to (a3) respectively. (c1) to (c3) Summed distribution of edge states in (a1) to (a3) respectively. (d1) to (d3) Element $|G_{mn}|$ of the Green's function for (a1) to (a3). For each case, reference energy is chosen to be $E_r = -1$, which is enclosed by the boundary loop spectrum in (a1) and (a2). n is chosen as the top-left corner site for each hexagonal lattice, and $m = (x, y)$ ranges across all lattice sites. Other parameters are $t_a = 0.25$, $t_b = 1$, and $\alpha = 0.5$.

Removing lattice sites on each corner divides 1D boundary of the triangle geometry into three disconnected segments. Similar with the trapezoidal geometry, the top geometric edge of each corner of a hexagonal lattice acts as a part of its physical bulk, and bulk states of the system show vanishing distribution only along the other three edges [Figs. S1(b1)-(b3)]. Edge states in hexagonal lattices are also seen to exhibit a clear accumulation at one side of each of these edges, i.e. three of the six corners of a hexagonal lattice, [Figs. S1(c1)-(c3)]. When Q increases, areas with nontrivial boundary spectral winding in the complex energy plane shrink and eventually become some lines [Fig. S1(a3)]. Meanwhile, localization of these corner states also become stronger, which can be seen from larger values of FD [brighter color from Fig. S1(c1) to (c3)]. As discussed in the main text, vanishing boundary spectral winding and strong corner localization in Fig. S1(a3) and (c3) indicate the emergence of an OBC type of HSTE.

In the main text, we have argued that in a trapezoid lattice, the two ends of its physical edge are (weakly) connected when only a few rows (e.g $M = 5$) of lattice sites are removed from the top corner of its parent triangle lattice. This intuitive picture can be more clearly seen in hexagonal lattices, whose physical edge breaks into three segments. To see this, we consider the amplitudes of elements G_{mn} of the Green's function $G = 1/(E_r - H)$, with E_r a reference energy chosen to be enclosed by the

boundary spectrum. As discussed in the main text, This quantity describes the strength of a response field at site m to a driven field at site n [19, 20]. Here we have chosen n to be the top-left corner of the hexagonal lattices, and illustrated $|G_{mn}|$ for all sites in the lattices. It is seen in Fig. S1(d1) and (d2) that in the presence of nontrivial boundary winding, $|G_{mn}|$ presents a peak at the top-right corner of the lattices, suggesting that an input signal travels through all edges and is amplified maximally on this corner site. On the other hand, when nontrivial boundary winding vanishes, $|G_{mn}|$ reaches its maximal value at the bottom-left corner, i.e. the other end of the left physical edge, suggesting that it is disconnected from the rest edges and behaves as an OBC non-Hermitian chain [Fig. S1(d3)]. The exponentially increasing $|G_{mn}|$ also indicates a directional/chiral signal amplification as in an actual 1D system. The amplification ratio $\text{Max}[|G_{mn}|]$ is seen to be much smaller in Fig. S1(d1), which is also in consistence to the understanding that in this case, the edges are more closer to a 1D PBC non-Hermitian chain, which does not support a directional amplification.

TOPOLOGICAL BOUNDARY RESPONSE FOR DIFFERENT GEOMETRIES

In the main text, we consider a topological response to detect the boundary spectral winding of our systems, namely a response on a boundary lattice site to a local driving field on a neighboring site, with a local perturbation introduced the hopping connecting these two sites. A one-on-one correspondence is established between the boundary spectral winding and a response quantity defined as

$$\nu_{mn}(\beta) = \partial \ln |G_{mn}(\beta)| / \partial \beta,$$

with β a parameter controlling the perturbation to a boundary hopping ($t' \rightarrow e^{-\beta} t'$), G_{mn} an element of the Green's function $G(\beta) = 1/[E_r - H(\beta)]$, E_r a reference energy for defining the boundary spectral winding, and (m, n) labeling the response and driven lattice sites respectively.

Intuitively, these two sites can be chosen arbitrarily along edges, except for those in the top edge of a trapezoid lattice, which belongs to the physical bulk of the system. In Fig. 4 in the main text, the response and driven lattice sites are chosen from the middle unit cell in the bottom of the lattice. In Fig. S2, we demonstrate the same results as in Fig. 4(c), but with the response and driven lattice sites chosen from left and top edge respectively. It is seen that the response quantity ν_{mn} still manifests the boundary spectral winding accurately for the former case, but not for the latter case.

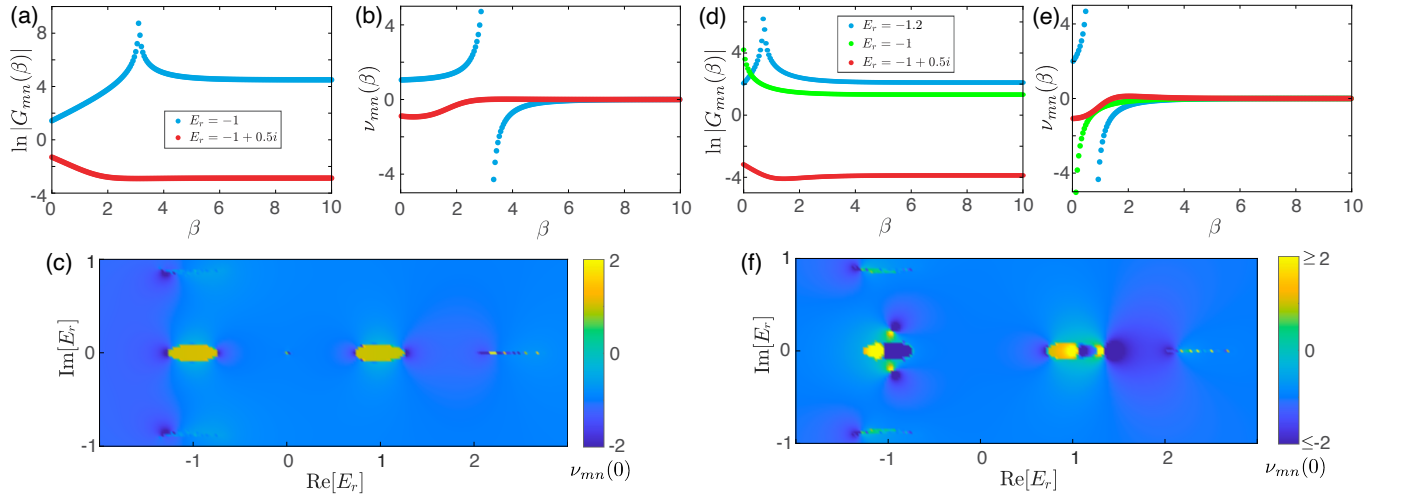


FIG. S2. (a) Element $G_{mn}(\beta)$ of the Green's function for the same trapezoidal lattice as in Fig. 3(d) in the main text, for different reference energies E_r enclosed by the loop-like boundary spectrum (blue dots), and within the gap (red dots) respectively. The lattice contains 25 rows of unit cells and 30 unit cells in the last row, with the top lattice site removed in each unit cell in the top row. m and n are chosen as the top and bottom-left sites of the first unit cell in the 13th last row, i.e. two edge sites in the middle unit cell of left edge of the trapezoid lattice. (b) Topological response $\nu_{mn}(\beta)$ for the same system and parameters as in (a). (c) Topological response $\nu_{mn}(\beta)$ at $\beta = 0$ for the same system with different E_r . (d) to (f) the same results as in (a) to (c), only with m and n chosen to be the bottom-right and -left sites of the third unit cell in the top row of the lattices, i.e. two edge sites in the middle unit cell of top edge of the trapezoid lattice. In panel (d) and (e), both green and blue dots correspond to E_r enclosed by the loop-like boundary spectrum. Other parameters are $L = 30$, $M = 5$, $t_a = 0.25$, $t_b = 1.0$, $\alpha = 0.5$.

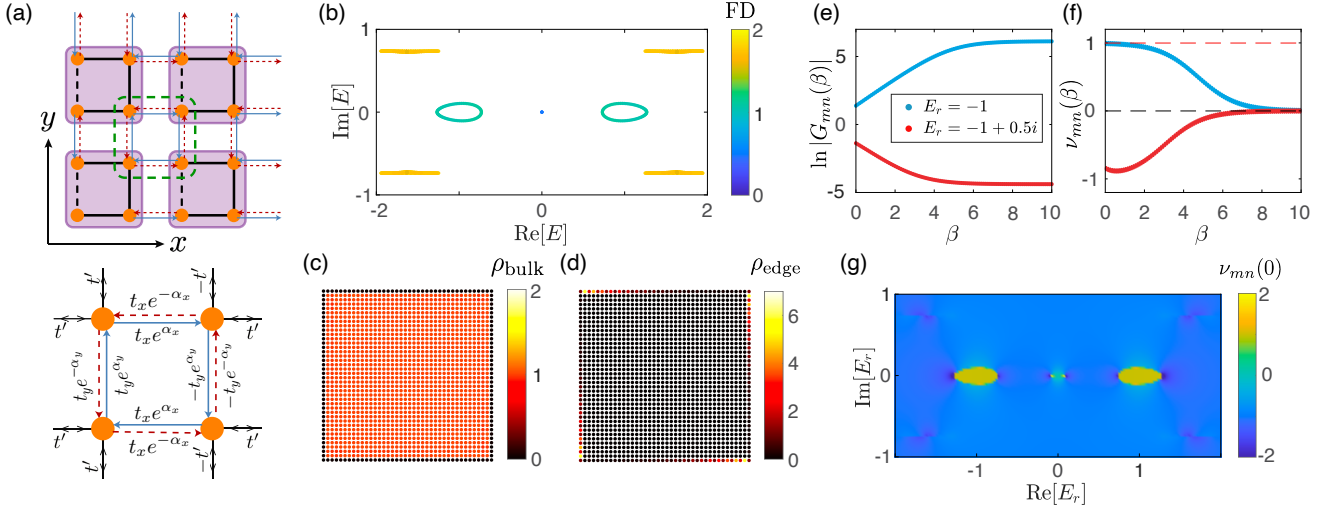


FIG. S3. (a) Sketch of the non-Hermitian BBH model. (b) Energy spectra of non-Hermitian BBH model with $L_x = L_y = 20$, colors indicate the FD of each eigenstate. (c) and (d) Summed distribution of bulk states and edge states respectively. Other parameters are $t_x = t_y = 0.25$, $t' = 1.0$, $\alpha_x = \alpha_y = 0.5$. (e) Element $G_{mn}(\beta)$ of the Green's function of the non-Hermitian BBH model, with m and n chosen as the bottom-left and -right sites of the 11th unit cell in the bottom row of the lattices, and a perturbed hopping parameter $t' \rightarrow e^{-\beta}t'$ between these two sites. Reference energies E_r are chosen to be enclosed by the loop-like boundary spectrum (blue dots), and within the gap (red dots) respectively. (f) Topological response $\nu_{mn}(\beta)$ for the same system and parameters as in (e). (g) Topological response $\nu_{mn}(\beta)$ at $\beta = 0$.

BOUNDARY SPECTRAL WINDING IN NON-HERMITIAN BENALCAZAR-BERNEVIG-HUGHES MODEL

In this section we consider another example, namely the non-Hermitian Benalcazar-Bernevig-Hughes (BBH) model [55, 56] as shown in Fig. S3(a), which also support nontrivial boundary spectral winding in certain parameter regimes. Its bulk Hamiltonian reads

$$H(\mathbf{k}) = \begin{pmatrix} 0 & t' + t_x^- e^{-ik_x} & -t' - t_y^+ e^{ik_y} & 0 \\ t' + t_x^+ e^{ik_x} & 0 & 0 & t' + t_y^- e^{ik_y} \\ -t' - t_y^- e^{-ik_y} & 0 & 0 & t' + t_x^+ e^{-ik_x} \\ 0 & t' + t_y^+ e^{-ik_y} & t' + t_x^- e^{ik_x} & 0 \end{pmatrix}, \quad (\text{S1})$$

where $t_x^\pm = t_x e^{\pm\alpha_x}$ and $t_y^\pm = t_y e^{\pm\alpha_y}$ represent asymmetric intercell hopping parameters along \hat{x} and \hat{y} directions respectively, and t' is the amplitude of intracell Hermitian hopping. In the Hermitian scenario with $\alpha_x = \alpha_y = 0$, the BBH model supports both 1st-order edge states and 2nd-order corner states.

The non-Hermitian BBH model we construct can be viewed as a combination of four sets of non-Hermitian SSH chains along two different directions (\hat{x}, \hat{y}). In each direction, two different SSH chains are chosen to have opposite non-reciprocity, leading to destructive interference of non-reciprocity in the bulk. FD is close to 2 for eigenstates in four bulk bands (orange color) for the system with a rectangle geometry [Fig. S3(b)], and the summed bulk distribution $\rho_{\text{bulk}}(\mathbf{r})$ distributes uniformly in the 2D bulk [Fig. S3(c)], indicating the absence of NHSE for bulk states. Similar to the non-Hermitian breathing Kagome lattice with triangle geometry in the main text, the non-Hermitian BBH model we construct also has nontrivial boundary spectral winding [Fig. S3(b)], as its four edges support non-reciprocity toward the same chiral direction. Numerically, we observe a weak eigenstate accumulation toward these corners along edges of the 2D system [Fig. S3(d)].

To detect the boundary spectral winding, we consider a topological response to an external local driving field, as discussed in the main text. Specifically, a perturbation is introduced to the amplitude of one intra-cell hopping along the system's 1D boundary,

$$t' \rightarrow t' e^{-\beta},$$

and we calculate the Green's function as $G(\beta) = 1/[E_r - H(\beta)]$. As shown in Fig. S3(e), The topological response associated with boundary spectral winding can be extracted from an element of the Green's function G_{mn} , with m and n labeling the two lattice sites connected by the perturbed hopping. As seen in Fig. S3(e), G_{mn} increases with β and eventually stops at a large constant value for a reference energy enclosed by the left loop-like boundary spectrum ($E_r = -1$). In contrast, G_{mn} decreases to a small value for a reference energy outside the boundary spectrum ($E_r = -1 + 0.5i$). The topological response quantity

$\nu_{mn}(\beta) = \partial \ln |G_{mn}(\beta)| / \partial \beta$ also exhibits distinguished behaviors for different E_r , as shown in Fig. S3(f), offering a way to detect the boundary spectral winding. Therefore we scan E_r for a parameter regime covering the system's full spectrum, and demonstrate the value of $\nu_{mn}(\beta)$ at $\beta = 0$ in Fig. S3(g). As expected, the region with nontrivial boundary spectral winding is characterized by $\nu_{mn}(0) \simeq 1$, while other regions generally have a non-positive $\nu_{mn}(0)$.

* lilh56@mail.sysu.edu.cn

- [1] M Zahid Hasan and Charles L Kane, "Colloquium: topological insulators," *Rev. Mod. Phys.* **82**, 3045 (2010).
- [2] Xiao-Liang Qi and Shou-Cheng Zhang, "Topological insulators and superconductors," *Rev. Mod. Phys.* **83**, 1057 (2011).
- [3] Shunyu Yao and Zhong Wang, "Edge states and topological invariants of non-hermitian systems," *Phys. Rev. Lett.* **121**, 086803 (2018).
- [4] Shunyu Yao, Fei Song, and Zhong Wang, "Non-hermitian chern bands," *Phys. Rev. Lett.* **121**, 136802 (2018).
- [5] Dan S. Borgnia, Alex Jura Kruchkov, and Robert-Jan Slager, "Non-hermitian boundary modes and topology," *Phys. Rev. Lett.* **124**, 056802 (2020).
- [6] Kai Zhang, Zhesen Yang, and Chen Fang, "Correspondence between winding numbers and skin modes in non-hermitian systems," *Phys. Rev. Lett.* **125**, 126402 (2020).
- [7] Nobuyuki Okuma, Kohei Kawabata, Ken Shiozaki, and Masatoshi Sato, "Topological origin of non-hermitian skin effects," *Phys. Rev. Lett.* **124**, 086801 (2020).
- [8] Tony E. Lee, "Anomalous edge state in a non-hermitian lattice," *Phys. Rev. Lett.* **116**, 133903 (2016).
- [9] Ye Xiong, "Why does bulk boundary correspondence fail in some non-hermitian topological models," *Journal of Physics Communications* **2**, 035043 (2018).
- [10] Flore K. Kunst, Elisabet Edvardsson, Jan Carl Budich, and Emil J. Bergholtz, "Biorthogonal bulk-boundary correspondence in non-hermitian systems," *Phys. Rev. Lett.* **121**, 026808 (2018).
- [11] Kazuki Yokomizo and Shuichi Murakami, "Non-bloch band theory of non-hermitian systems," *Physical review letters* **123**, 066404 (2019).
- [12] Zhesen Yang, Kai Zhang, Chen Fang, and Jiangping Hu, "Non-hermitian bulk-boundary correspondence and auxiliary generalized brillouin zone theory," *Physical Review Letters* **125**, 226402 (2020).
- [13] Ching Hua Lee and Ronny Thomale, "Anatomy of skin modes and topology in non-hermitian systems," *Phys. Rev. B* **99**, 201103 (2019).
- [14] Loic Herviou, Jens H. Bardarson, and Nicolas Regnault, "Defining a bulk-edge correspondence for non-hermitian hamiltonians via singular-value decomposition," *Physical Review A* **99**, 052118 (2019).
- [15] Stefano Longhi, "Topological phase transition in non-hermitian quasicrystals," *Physical Review Letters* **122**, 237601 (2019).
- [16] Hui Jiang, Li-Jun Lang, Chao Yang, Shi-Liang Zhu, and Shu Chen, "Interplay of non-hermitian skin effects and anderson localization in nonreciprocal quasiperiodic lattices," *Physical Review B* **100**, 054301 (2019).
- [17] Fei Song, Shunyu Yao, and Zhong Wang, "Non-hermitian skin effect and chiral damping in open quantum systems," *Physical review letters* **123**, 170401 (2019).
- [18] Fei Song, Shunyu Yao, and Zhong Wang, "Non-hermitian topological invariants in real space," *Physical Review Letters* **123**, 246801 (2019).
- [19] Clara C Wanjura, Matteo Brunelli, and Andreas Nunnenkamp, "Topological framework for directional amplification in driven-dissipative cavity arrays," *Nature communications* **11**, 1–13 (2020).
- [20] Wen-Tan Xue, Ming-Rui Li, Yu-Min Hu, Fei Song, and Zhong Wang, "Simple formulas of directional amplification from non-bloch band theory," *Physical Review B* **103**, L241408 (2021).
- [21] Clara C. Wanjura, Matteo Brunelli, and Andreas Nunnenkamp, "Correspondence between non-hermitian topology and directional amplification in the presence of disorder," *Phys. Rev. Lett.* **127**, 213601 (2021).
- [22] Jan Carl Budich and Emil J. Bergholtz, "Non-hermitian topological sensors," *Phys. Rev. Lett.* **125**, 180403 (2020).
- [23] Kai Wang, Avik Dutt, Ki Youl Yang, Casey C Wojcik, Jelena Vučković, and Shanhui Fan, "Generating arbitrary topological windings of a non-hermitian band," *Science* **371**, 1240–1245 (2021).
- [24] Stefano Longhi, "Self-healing of non-hermitian topological skin modes," *Phys. Rev. Lett.* **128**, 157601 (2022).
- [25] Sen Mu, Ching Hua Lee, Linhu Li, and Jiangbin Gong, "Emergent fermi surface in a many-body non-hermitian fermionic chain," *Phys. Rev. B* **102**, 081115 (2020).
- [26] Ching Hua Lee, Linhu Li, Ronny Thomale, and Jiangbin Gong, "Unraveling non-hermitian pumping: Emergent spectral singularities and anomalous responses," *Phys. Rev. B* **102**, 085151 (2020).
- [27] Ching Hua Lee, "Exceptional bound states and negative entanglement entropy," *Physical Review Letters* **128**, 010402 (2022).
- [28] Cui-Xian Guo, Chun-Hui Liu, Xiao-Ming Zhao, Yanxia Liu, and Shu Chen, "Exact solution of non-hermitian systems with generalized boundary conditions: Size-dependent boundary effect and fragility of the skin effect," *Phys. Rev. Lett.* **127**, 116801 (2021).
- [29] Yifei Yi and Zhesen Yang, "Non-hermitian skin modes induced by on-site dissipations and chiral tunneling effect," *Phys. Rev. Lett.* **125**, 186802 (2020).
- [30] Linhu Li, Ching Hua Lee, and Jiangbin Gong, "Impurity induced scale-free localization," *Communications Physics* **4**, 1–9 (2021).
- [31] Linhu Li, Ching Hua Lee, and Jiangbin Gong, "Geometric characterization of non-hermitian topological systems through the singularity ring in pseudospin vector space," *Physical Review B* **100**, 075403 (2019).
- [32] Linhu Li, Ching Hua Lee, Sen Mu, and Jiangbin Gong, "Critical non-hermitian skin effect," *Nature communications* **11** (2020).
- [33] Linhu Li, Sen Mu, Ching Hua Lee, and Jiangbin Gong, "Quantized classical response from spectral winding topology," *Nature communications* **12**, 5294 (2021).

- [34] Yanxia Liu, Yumeng Zeng, Linhu Li, and Shu Chen, “Exact solution of the single impurity problem in nonreciprocal lattices: Impurity-induced size-dependent non-hermitian skin effect,” *Phys. Rev. B* **104**, 085401 (2021).
- [35] Hui-Qiang Liang, Sen Mu, Jiangbin Gong, and Linhu Li, “Anomalous hybridization of spectral winding topology in quantized steady-state responses,” *Physical Review B* **105**, L241402 (2022).
- [36] Linhu Li and Ching Hua Lee, “Non-hermitian pseudo-gaps,” *Science Bulletin* **67**, 685–690 (2022).
- [37] Xiao-Qi Sun, Penghao Zhu, and Taylor L. Hughes, “Geometric response and disclination-induced skin effects in non-hermitian systems,” *Phys. Rev. Lett.* **127**, 066401 (2021).
- [38] Balaganchi A. Bhargava, Ion Cosma Fulga, Jeroen van den Brink, and Ali G. Moghaddam, “Non-hermitian skin effect of dislocations and its topological origin,” *Phys. Rev. B* **104**, L241402 (2021).
- [39] Frank Schindler and Abhinav Prem, “Dislocation non-hermitian skin effect,” *Phys. Rev. B* **104**, L161106 (2021).
- [40] Archisman Panigrahi, Roderich Moessner, and Bitan Roy, “Non-hermitian dislocation modes: Stability and melting across exceptional points,” *Phys. Rev. B* **106**, L041302 (2022).
- [41] Kai Zhang, Zhesen Yang, and Chen Fang, “Universal non-hermitian skin effect in two and higher dimensions,” *Nature communications* **13**, 2496 (2022).
- [42] Hui Jiang and Ching Hua Lee, “Dimensional transmutation from non-hermiticity,” 2207.08843v2.
- [43] Ching Hua Lee, Linhu Li, and Jiangbin Gong, “Hybrid higher-order skin-topological modes in nonreciprocal systems,” *Phys. Rev. Lett.* **123**, 016805 (2019).
- [44] Linhu Li, Ching Hua Lee, and Jiangbin Gong, “Topological switch for non-hermitian skin effect in cold-atom systems with loss,” *Physical Review Letters* **124**, 250402 (2020).
- [45] Yaohua Li, Chao Liang, Chenyang Wang, Cuicui Lu, and Yong-Chun Liu, “Gain-loss-induced hybrid skin-topological effect,” *Phys. Rev. Lett.* **128**, 223903 (2022).
- [46] Weiwei Zhu and Jiangbin Gong, “Hybrid skin-topological modes without asymmetric couplings,” *Phys. Rev. B* **106**, 035425 (2022).
- [47] Kohei Kawabata, Masatoshi Sato, and Ken Shiozaki, “Higher-order non-hermitian skin effect,” *Phys. Rev. B* **102**, 205118 (2020).
- [48] Yongxu Fu, Jihan Hu, and Shaolong Wan, “Non-hermitian second-order skin and topological modes,” *Phys. Rev. B* **103**, 045420 (2021).
- [49] Ryo Okugawa, Ryo Takahashi, and Kazuki Yokomizo, “Second-order topological non-hermitian skin effects,” *Phys. Rev. B* **102**, 241202 (2020).
- [50] W. P. Su, J. R. Schrieffer, and A. J. Heeger, “Solitons in polyacetylene,” *Phys. Rev. Lett.* **42**, 1698–1701 (1979).
- [51] Simon Lieu, “Topological phases in the non-hermitian su-schrieffer-heeger model,” *Physical Review B* **97**, 045106 (2018).
- [52] Chuanhao Yin, Hui Jiang, Linhu Li, Rong Lü, and Shu Chen, “Geometrical meaning of winding number and its characterization of topological phases in one-dimensional chiral non-hermitian systems,” *Phys. Rev. A* **97**, 052115 (2018).
- [53] “Supplemental materials,” *Supplemental Materials*.
- [54] Deyuan Zou, Tian Chen, Wenjing He, Jiacheng Bao, Ching Hua Lee, Houjun Sun, and Xiangdong Zhang, “Observation of hybrid higher-order skin-topological effect in non-hermitian topoelectrical circuits,” *Nature Communications* **12**, 1–11 (2021).
- [55] Wladimir A Benalcazar, B Andrei Bernevig, and Taylor L Hughes, “Quantized electric multipole insulators,” *Science* **357**, 61–66 (2017).
- [56] Wladimir A. Benalcazar, B. Andrei Bernevig, and Taylor L. Hughes, “Electric multipole moments, topological multipole moment pumping, and chiral hinge states in crystalline insulators,” *Phys. Rev. B* **96**, 245115 (2017).